Draft version August 28, 2020
Typeset using LATEX **twocolumn** style in AASTeX62

Detecting H II Regions in the Outer Scutum-Centaurus Arm

A. Johnson[1,2] and W. P. Armentrout[2]

[1]*Pacific Lutheran University*
[2]*Green Bank Observatory*

ABSTRACT

The Outer Scutum-Centaurus (OSC) spiral arm was discovered by Dame & Thaddeus (2011) and is the most distant molecular spiral arm in the Galaxy. Lying about 15 kpc from the center of the Galaxy and warping up to 4° above the Galactic plane at its peak, the OSC has been excluded from the scope of many surveys of the Galactic plane, which are typically confined to within one degree of the Galactic plane. In this study, we continue in a similar research direction as Armentrout et al. (2017). Of the 12 sources we observe, 7 are re-observations of previously covered sources from Armentrout et al. (2017). The other 5 are sources with no previously established 10 GHz radio continuum data. We identify 10 GHz radio continuum associated with 7 observed OSC H II regions. By assuming one dominant ionizing source, we are able to assign spectral types from O9 to O5.5 for these sources. We also establish upper limits for the RMS associated with the other 5 nondetections in our study. Combined with existing data from Armentrout et al. (2017), we identify a total of 12 existing H II regions in the OSC Arm, with spectral types ranging from O9 to O4. Further research could involve re-observing the nondetections for longer periods and applying different cleaning and smoothing parameters the images in an effort to find the method with the lowest RMS as possible, raising the accuracy of continuum data.

Keywords: H II Regions, Galactic Structure, GBT.

1. INTRODUCTION

Galactic H II regions are areas of ionized hydrogen surrounding massive stars. High-mass stars emit large amounts of ionizing photons ($\lambda < 91.2$ nm) which are able to completely ionize their surrounding interstellar hydrogen. These star-forming regions have short lifespans (∼10 Myr), and as such are zero-age objects compared to the age of the Milky Way. Consequently, they can be used to track star formation in the current epoch (Armentrout et al. 2017). Only high-mass stars can form an H II region, so they trace massive star formation (Anderson et al. 2014a). H II regions often have additional dense gas tracers from the molecular gas used in star formation, such as HCO, HCN, and CO, which can be used to confirm the existence of such a region. However, these tracers appear in more than just Galactic H II regions, so their existence isn't a guarantee of active star formation, but is rather an additional indicator of star formation activity.

Corresponding author: A. Johnson
johnson.business860@gmail.com

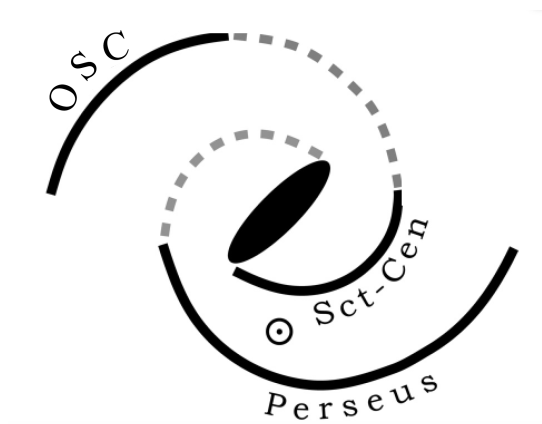

Figure 1. Galactic overhead image showing the position of the Outer Scutum-Centarus spiral arm (modified from Dame & Thaddeus (2011)).

1.1. H II *Regions*

H II regions emit such a powerful signal due to the interaction between electrons and the ionized region of hydrogen surrounding a massive star. As an electron passes by a positive hydrogen ion, Coulomb forces accelerate the electron, a process known as free-free radiation. It is so named because the passing electron is free both before and after the interaction, rather than getting captured by the ion (Condon & Ransom 2016). Most Galactic hydrogen is in its molecular form H_2, so the areas of ionized hydrogen surrounding massive stars (known as Strömgren spheres) are easily noticeable against the Galactic background. H II regions can be detected across the galaxy and are the brightest objects in the Milky Way observable in the infrared and radio spectra (Anderson et al. 2014a).

1.2. *Galactic Structure*

H II regions typically form in spiral arms due to the higher concentrations of interstellar gases. Due to their relatively short lifetimes, the high-mass stars at the core of H II regions tend to stay more or less in one place. Using this knowledge, the observation of H II regions is exceptionally useful in researching Galactic structure and evolution, such as in the case of the Outer Scutum-Centarus Arm (OSC), the furthest known molecular spiral arm of the Galaxy (Armentrout et al. 2017). The Milky Way is assumed to be a symmetric barred spiral by most models, warping upward at the outer reaches of the First Quadrant. This means that the furthest edges of the Milky Way should be noticeable at a significant ($\sim 4°$) angle above or below the Galactic plane, which is exactly how the first large-scale structures in the OSC were first discovered by Dame & Thaddeus (2011). The fact that it lies slightly outside of the plane means that observations can be exceptionally clear of interference compared to an observation taken at a completely flat angle, filled with thousands of parsecs of other gases and sources of random noise. The OSC may be one of the outermost star-forming regions in the Galaxy, with tens of distinct H II regions detected, detailed further in Armentrout et al. (2017), Anderson et al. (2014b), and Wenger et al. (2018).

2. OBSERVATIONS

We target every H II region from the *Wide-Field Infrared Survey Explorer (WISE)* catalog (Anderson et al. 2014a) with a velocity placing it in the OSC that did not already have continuum detections from Armentrout et al. (2017). A subset of 7 of these sources were part of the 12 sources observed in 2014, but were not detected in that study. We used J1822−0938 and J1922+1530 for gain calibrators, J1733-1304 as our bandpass calibrator, and 3C286 as our flux density calibrator. Observations (project code VLA 20A-495) were taken in June 2020, using the VLA in C-configuration at a central frequency of ∼9 GHz. Observations were taken for 3 minutes on-source at X-band, with a synthesized beamwidth of 2.1 arcsec and the largest angular scale at 145 arcsec. The data from Armentrout et al. (2017) we used (project code VLA 14A-194) were taken from July-August 2014 using the VLA in D-configuration at two overlapping frequencies covering 8.012-10.041 GHz. Observations were taken for 4 minutes on-source at X-band, with a synthesized beamwidth of 7.2 arcsec and the largest angular scale at 145 arcsec.

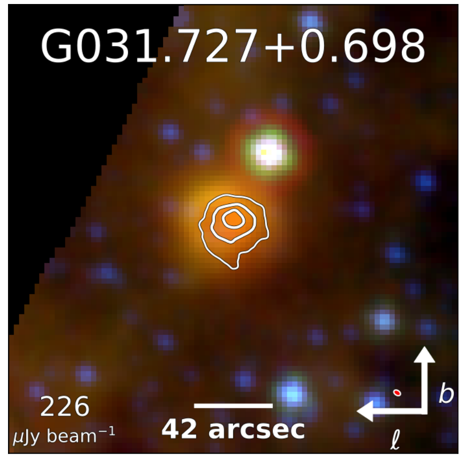

Figure 2. Infrared and radio image of one of the candidate H II regions observed with the VLA. WISE bands w2 (4.6 µm), w3 (12 µm), and w4 (22 µm) are represented by blue, green, and red respectively. VLA radio continuum obtained in C configuration (project code 20A-495) were smoothed using a 15 arcsec "boxcar" filtering model. Contours of the smoothed VLA data are placed at 33%, 66%, and 90% peak radio continuum flux for sources detected in radio continuum. The beam resolution is shown in the bottom right, and scale bars represent the regions' angular sizes as catalogued in the WISE Catalog of Galactic H II Regions (Anderson et al. 2014a). If an image appears to be a nondetection using VLA radio continuum data, a "∅" symbol appears in the bottom left corner. We smoothed all radio data using a 15 arcsec "boxcar" model. For nondetections, RMS contours at 0.25, 0.5, 1, 2, and 3 times the RMS level are shown. The other source images are in Figures 6 and 7.

3. DATA ANALYSIS

We used VLA continuum data and WISE 3-color IR data to form images for 12 potential H II regions (see Figure 2). We plan in the future to combine our data with those from Armentrout et al. (2017) for any re-observed sources. We split individual source files from the full measurement set, then created a non-interactive first clean (dirty map) using CASA, and finally we ran a series of 3 interactive cleans to more accurately reduce RMS for each image and future computations. Then, using the CASA's viewer function, we hand-drew polygonal masks that best fit the center regions, for the images that had clear non-RMS flux. For any images that

Table 1. 10 GHz VLA Continuum Parameters

WISE Name	α_{J2000} hh:mm:ss	δ_{J2000} dd:mm:ss	σS_{peak} mJy beam^{-1}	S_{int} mJy	S_{peak} mJy beam^{-1}
G026.610−00.212	18:40:37.65	−05:43:16.2	8.595	142.293	11.421
G031.727+00.698	18:46:45.30	−00:45:14.2	0.140	9.256	0.238
G032.928+00.606	18:49:16.41	00:16:22.2	11.415	155.432	14.033
G040.287+01.151	19:00:47.40	07:04:09.8	0.015	...	...
G040.954+02.473	18:57:16.11	08:15:56.0	0.017	...	...
G041.304+01.997	18:59:37.53	08:21:36.4	0.929	9.856	1.001
G041.755+01.451	19:02:25.33	08:30:42.4	0.061	...	...
G041.804+01.503	19:02:19.55	08:34:44.8	0.049	19.064	0.106
G046.368+00.802	19:13:24.04	12:18:27.4	0.125	9.05	0.487
G061.085+02.502	19:36:39.45	26:04:02.5	0.014	...	...
G061.180+02.447	19:37:04.64	26:07:24.5	0.009	...	...
G062.578+02.387	19:40:22.49	27:18:42.8	2.907	123.949	3.591

Note—This table includes all 12 sources observed as part of VLA20A-495. Sources with "..." in the S_{int} and S_{peak} columns have measured background RMS, but no detected radio continuum.

were difficult to identify a clear center region, we created an RMS mask instead, which included the entire background area, excluding other strong sources in the field. Before running CASA's statistics function, we smoothed the images in a boxcar distribution across a radius of 15 arcsec. Finally, we were ready to pull continuum statistics from the observed mask regions using CASA's imstat routine, including peak flux, integrated flux over the entire masked region, and peak RMS. These results are detailed in Table 1.

For every detected H II region among these sources, we used the aforementioned continuum data as well as source velocities from WISE (Anderson et al. 2014a), Armentrout et al. (2017), and Wenger et al. (2018) to calculate kinematic distances based on two different Galactic rotation curve models, Brand & Blitz (1993) and Reid et al. (2014).

$$L_\nu = 4\pi\ 10^{-26} \left[\frac{D}{\mathrm{m}}\right]^2 \left[\frac{S_{int}}{\mathrm{Jy}}\right] [\mathrm{W\ Hz^{-1}}] \tag{1}$$

$$N_{Ly} = 6.3\times10^{52}\left[\frac{T_e}{10^4\ \mathrm{K}}\right]^{-0.45}\left[\frac{\nu}{\mathrm{GHz}}\right]^{0.1}\left[\frac{L_\nu}{10^{20}\ \mathrm{W\ Hz^{-1}}}\right][\mathrm{s^{-1}}] \tag{2}$$

Using the above equations (detailed in Section 5.3 of Armentrout et al. (2017)) for each rotation curve model, we were able to determine source luminosity and the amount of Lyman-continuum photons ionizing each region. With that information, we determined the spectral type of each detected H II region (assuming a singular stellar source) using a combination of models from Martins et al. (2005) and Smith et al. (2002), further explained in Armentrout et al. (2017). The results of the above processes are detailed in Table 2.

In order to visually represent the scope of our resulting data, we used background H I tracers from the Leiden-Argentine-Bonn (LAB) survey (Kalberla et al. 2005) following the OSC Arm to plot each source from this study and Armentrout et al. (2017), both from the view of an overhead observer and from within the Galactic plane (Figures 3 and 4).

In these figures, detections from this study are shown as filled red stars, detections from Armentrout et al. (2017) as open stars with red outlines, and nondetections from this study as an orange plus. We also created a different figure to visualize the data in a more quantitative way. Using PyPlot and MatPlotLib, we created a corner plot with individual scatter-style subplots comparing every relevant piece of continuum information against each other, as well as plotted best-fit lines for those data sets with an R^2 value greater than 0.33 in order to more clearly see trends and relations between various metrics. We further searched for trends in the corner plot by eventually combining GBT Dense Gas data with our new observations and the OSC H II region data from Armentrout et al. (2017).

4. COMPARISON WITH PREVIOUS LITERATURE

Using the SIMBAD Astronomical Database, VizieR database, and the archived papers linked to those sources, we conducted a literature search for known star clusters and H II regions in the areas of our 17 total OSC coordinates of interest. Existing continuum information corroborates values we calculated using CASA,

Table 2. Derived Region Parameters

WISE Name	V_{LSR}	Brand					Reid				
		R_{Gal}	D	Z	$\log_{10}(N_{Ly})$	Spectral	D	R_{Gal}	Z	$\log_{10}(N_{Ly})$	Spectral
	km s^{-1}	kpc	kpc	kpc	s^{-1}	Type	kpc	kpc	kpc	s^{-1}	Type
*G026.610−00.212	−35.7	13.77	20.84	−0.08	48.94	O6	14.9	22	−0.08	48.99	O5.5
G028.320+01.243	−44.0	15.25	22.18	0.48	47.97	O8.5	16.43	23.41	0.36	48.02	O8.5
*G031.727+00.698	−39.2	13.26	19.71	0.24	47.67	O9	14.37	20.89	0.25	47.72	O9
*G032.928+00.606	−38.3	12.89	19.16	0.20	48.97	O5.5	13.98	20.32	0.21	49.02	O5.5
G033.007+01.150	−57.6	17.05	23.54	0.47	48.18	O8	18.31	24.84	0.37	48.23	O8
G039.183−01.422	−51.0	13.88	19.39	−0.48	48.28	O8	15.01	20.61	−0.37	48.33	O7.5
*G040.287+01.151	−50.0	13.53	18.85	0.38	...	...	14.65	20.07	0.40	...	...
*G040.954+02.473	−52.5	13.82	19.07	0.82	...	...	14.95	20.29	0.88	...	...
*G041.304+01.997	−53.7	13.95	19.16	0.67	47.87	O9	15.08	20.39	0.71	47.93	O8.5
*G041.755+01.451	−54.8	14.04	19.19	0.49	...	...	15.18	20.43	0.52	...	...
*G041.804+01.503	−52.6	13.69	18.80	0.49	47.83	O9	14.82	20.03	0.53	47.88	O9
*G046.368+00.802	−59.9	14.09	18.55	0.26	47.58	O9	15.23	19.80	0.28	47.63	O9
G054.093+01.748	−85.3	16.99	20.52	0.63	48.06	O8.5	18.25	21.89	0.56	48.11	O8
G055.114+02.422	−76.1	15.26	18.43	0.78	49.28	O4	16.44	19.75	0.69	49.35	O4
*G061.085+02.502	−84.29	15.71	17.95	0.78	...	...	16.91	19.30	0.84	...	...
*G061.180+02.447	−84.81	15.77	18.00	0.77	...	...	16.99	19.37	0.83	...	...
*G062.578+02.387	−73.6	14.11	15.84	0.66	48.62	O7	15.26	17.18	0.72	48.69	O6.5

NOTE—This table includes all 17 sources in the *WISE* Catalog of Galactic H II Regions with a velocity placing it in the OSC. Starred sources were observed as part of VLA20A-495, while the remainder are from Armentrout et al. (2017). Sources with "..." in the N_{Ly} and Spectral Type columns have measured velocities, but no detected radio continuum. Spectral type is assigned based on a combination of models from Martins et al. (2005) and Smith et al. (2002).

but aside from that, no further relevant information was discovered nor used in our research.

5. RESULTS

In Table 1, the integrated flux, peak flux, and peak RMS continuum values calculated from each region observed as part of VLA20A-495 are listed, as well as their Galactic coordinate conversions into J2000 RA and Dec. Sources with "..." for flux values are nondetections, meaning that only the upper RMS limits for each region are significant data.

Table 2 includes all 17 sources in the *WISE* Catalog of Galactic H II Regions with a velocity placing it in the OSC. Data is from Armentrout et al. (2017) as well as data from VLA20A-495, showing the source velocity, various Galactic distances to the source, the $\log_{10}$ of the number of Lyman continuum photons emitted per second (calculated by Equations 1 and 2), and the resulting spectral type of the star powering the H II region (under the assumption that all of it is due to a single-star source, which is valid due to the logarithmic nature of spectral type classification). Spectral type is assigned based on a combination of models from Martins et al. (2005) and Smith et al. (2002). The full range of OSC H II region spectral types now stretches from O9 to O4, with 12 confirmed sources. Both the Brand and Reid rotation curves are used in calculations and displayed, which give slightly varying results but close enough to where the spectral types are either the same or within half of a type away, e.g. O6 to O6.5. Sources with "..." in the N_{Ly} and Spectral Type columns are nondetections and therefore have no meaningful data to display in those cells.

The source G062.578+02.387 does not appear to be in the region of the OSC we examined, as seen in Figure 3 (the bottom-most star outside of the grayscale H I background). This is likely an error on our part, due to having multiple listed source velocities. As such, it is still useful to examine due to the likelihood that it in fact rests in the OSC and provides information pertinent to star formation in the OSC.

There are several important interpretations we can make from this data. First, we are detecting several regions of high-mass star formation in the most distant molecular spiral arm of the Milky Way. From the data in Table 2 on these detected H II regions, we know that they are all extremely distant and have especially massive stars at their centers. Even the nondetections against the background RMS likely represent B-class star formation in fainter H II regions that we were unable to detect with this round of observations. Compared to the 2014 sample, we have identified even more H II regions as a result of our study, giving us more to analyze in the star-forming processes of the OSC's low-density, low-metallicity environment. The information gained by studying this region may ultimately shed light on similar processes in the outer edges of other disk galaxies.

6. SUMMARY AND FURTHER STUDY

With the data from this study, we were able to identify new radio continuum emission in 70 H II regions in the OSC Arm (up to spectral type of O5.5), as well as establishing upper limits for the RMS associated with our 5 observed nondetections. From these established upper limits of RMS, we know that the central star spectral type must be lower than what would correspond to our observed peak RMS. Combined with the previously existing data from Armentrout et al. 2017, this study brings the total of OSC H II regions with radio continuum and spectral type information up to 12. These OSC H II regions represent the most distant known high-mass star formation regions in the Milky Way and give us an excellent laboratory for studying star formation in the outer Galaxy. 5 observed regions were not detected with the VLA, and likely represent slightly lower-mass star formation (such as B-type stars, rather than O-type). These nondetections would benefit from longer VLA observations with reduced noise, which could potentially result in a detection of continuum for lower-mass stars.

Facilities: Green Bank Observatory

Software: Astropy, APLpy, CASA, GBTIDL

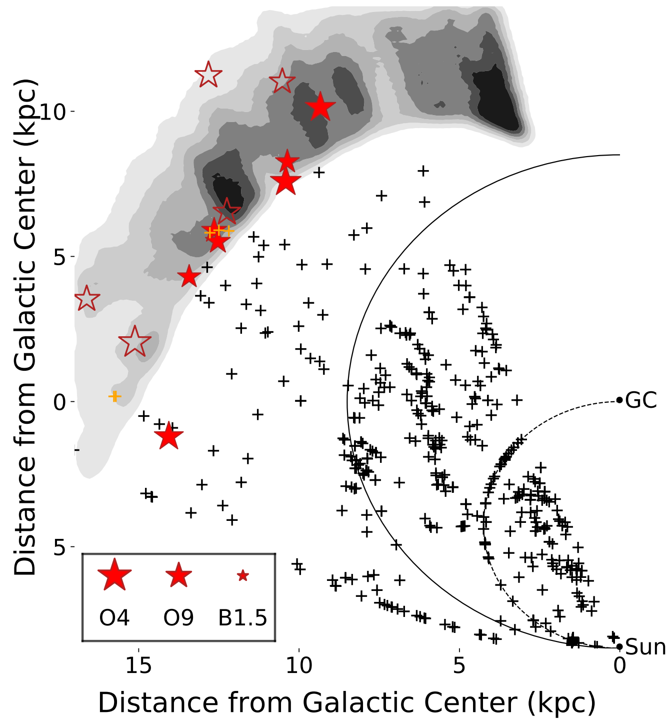

Figure 3. Face-on map of H II regions in the first Galactic quadrant. The Solar circle and tangent points are marked by solid and dashed lines, respectively. Black crosses mark H II regions from the WISE Catalog of Galactic H II Regions with known distances (Anderson et al. 2014a). We show nondetections from this study as orange pluses, confirmed H II regions from this study as filled red stars, and confirmed H II regions from Armentrout et al. (2017) as empty red stars. Stars indicate sources with detected radio continuum emission in addition to ammonia emission; these markers are scaled in size by stellar spectral type. Stars within the Solar circle suffer from the kinematic distance ambiguity (KDA), so both possible locations are plotted. We also show H I emission from the LAB survey following the arm in latitude and velocity, using a Brand rotation curve: $V_{LSR} = -1.6$ km s^{-1} deg$^{-1} \times \ell$, $b = 0.375° + 0.075 \times \ell$. This figure is modified from Armentrout et al. (2017).

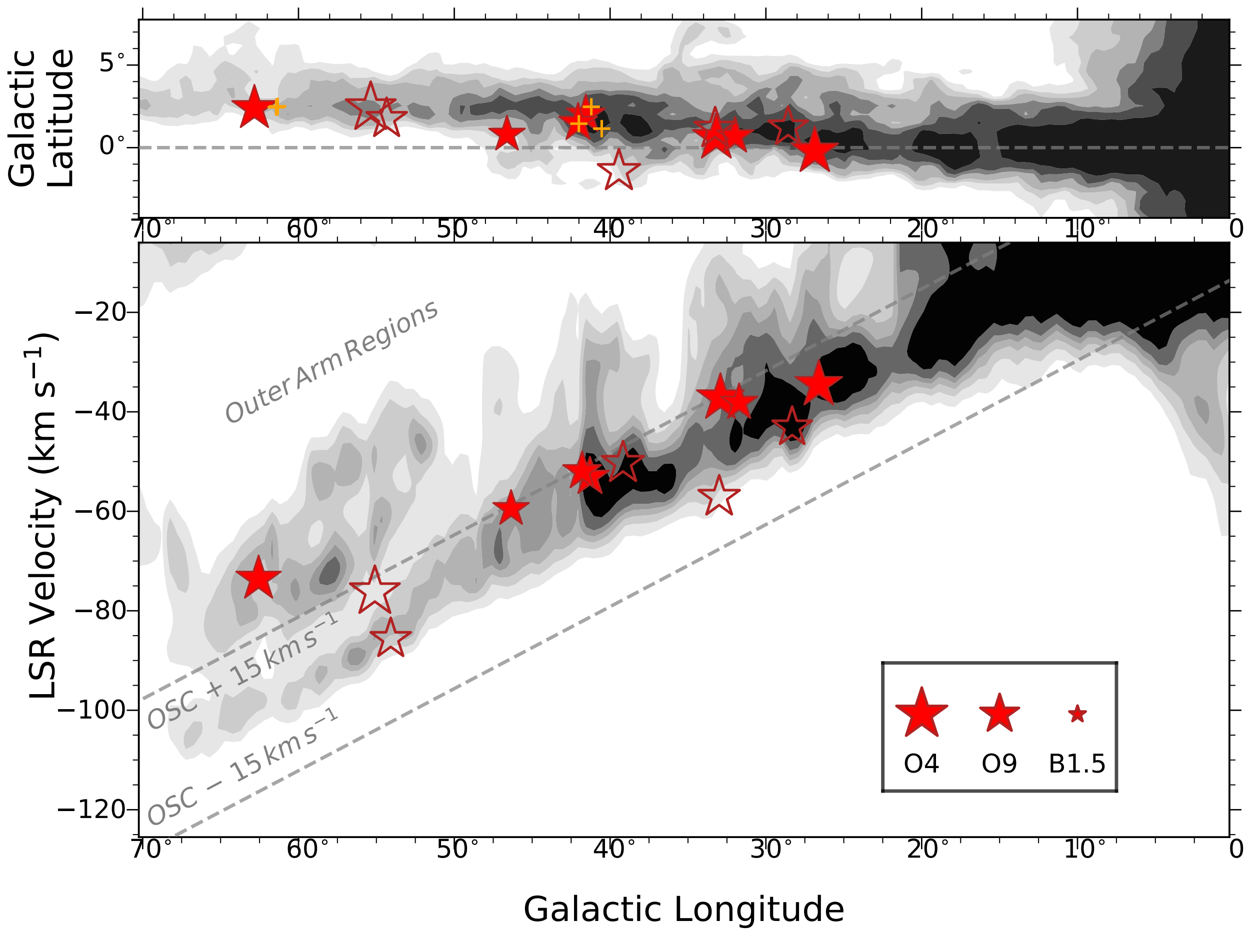

Figure 4. The Outer Scutum-Centaurus Arm as traced by integrated HI emission. **Top:** Velocity-integrated H I emission tracing the OSC arm, summed over a 14 km s^{-1} wide window following the center velocity given by $V_{LSR} = -1.6$ km s^{-1} deg^{-1} $\times\, \ell$. Overlaid are all observed H II region targets identified in Armentrout et al. (2017) and this study. We show nondetections from this study as orange pluses, confirmed H II regions from this study as filled red stars, and confirmed H II regions from Armentrout et al. (2017) as empty red stars. For detections, these markers are scaled by stellar type. **Bottom:** Longitude-velocity diagram of HI emission, summed over a 3.5° window following the arm in latitude according to $b = 0.375° + 0.075 \times \ell$. Overlaid are detected OSC H II regions from the same studies and with the same symbols as the top panel. Dashed lines indicate the central locus of the OSC in (ℓ, v) space as indicated by Dame & Thaddeus (2011), $V_{LSR} = -1.6$ km s^{-1} deg^{-1} $\times\, \ell \pm 15\,\mathrm{km\,s^{-1}}$. This figure is modified from Armentrout et al. (2017).

REFERENCES

Anderson, L. D., Bania, T. M., Balser, D. S., et al. 2014a, ApJS, 212, 1, doi: 10.1088/0067-0049/212/1/1

Anderson, L. D., Deharveng, L., Zavagno, A., et al. 2014b, ArXiv e-prints. https://arxiv.org/abs/1412.6470

Armentrout, W. P., Anderson, L. D., Balser, D. S., et al. 2017, ApJ, 841, 121, doi: 10.3847/1538-4357/aa71a1

Brand, J., & Blitz, L. 1993, A&A, 275, 67

Condon, J. J., & Ransom, S. M. 2016, Essential Radio Astronomy (Princeton University Press)

Dame, T. M., & Thaddeus, P. 2011, ApJL, 734, L24+, doi: 10.1088/2041-8205/734/1/L24

Kalberla, P. M. W., Burton, W. B., Hartmann, D., et al. 2005, A&A, 440, 775, doi: 10.1051/0004-6361:20041864

Martins, F., Schaerer, D., & Hillier, D. J. 2005, A&A, 436, 1049, doi: 10.1051/0004-6361:20042386

Reid, M. J., Menten, K. M., Brunthaler, A., et al. 2014, ApJ, 783, 130, doi: 10.1088/0004-637X/783/2/130

Smith, L. J., Norris, R. P. F., & Crowther, P. A. 2002, MNRAS, 337, 1309, doi: 10.1046/j.1365-8711.2002.06042.x

Wenger, T. V., Khan, A. A., Ferraro, N. G., et al. 2018, ApJ, 852, 2, doi: 10.3847/1538-4357/aa9bdb

APPENDIX

Figure 5 shows comparisons between each of the various metrics from our 10 GHz Radio continuum emissions and dense gas data, with best fit lines on especially well-correlated plots. Figures 6 and 7 show IR images of sources overlaid with radio contours. For more information, see description of Figure 2.

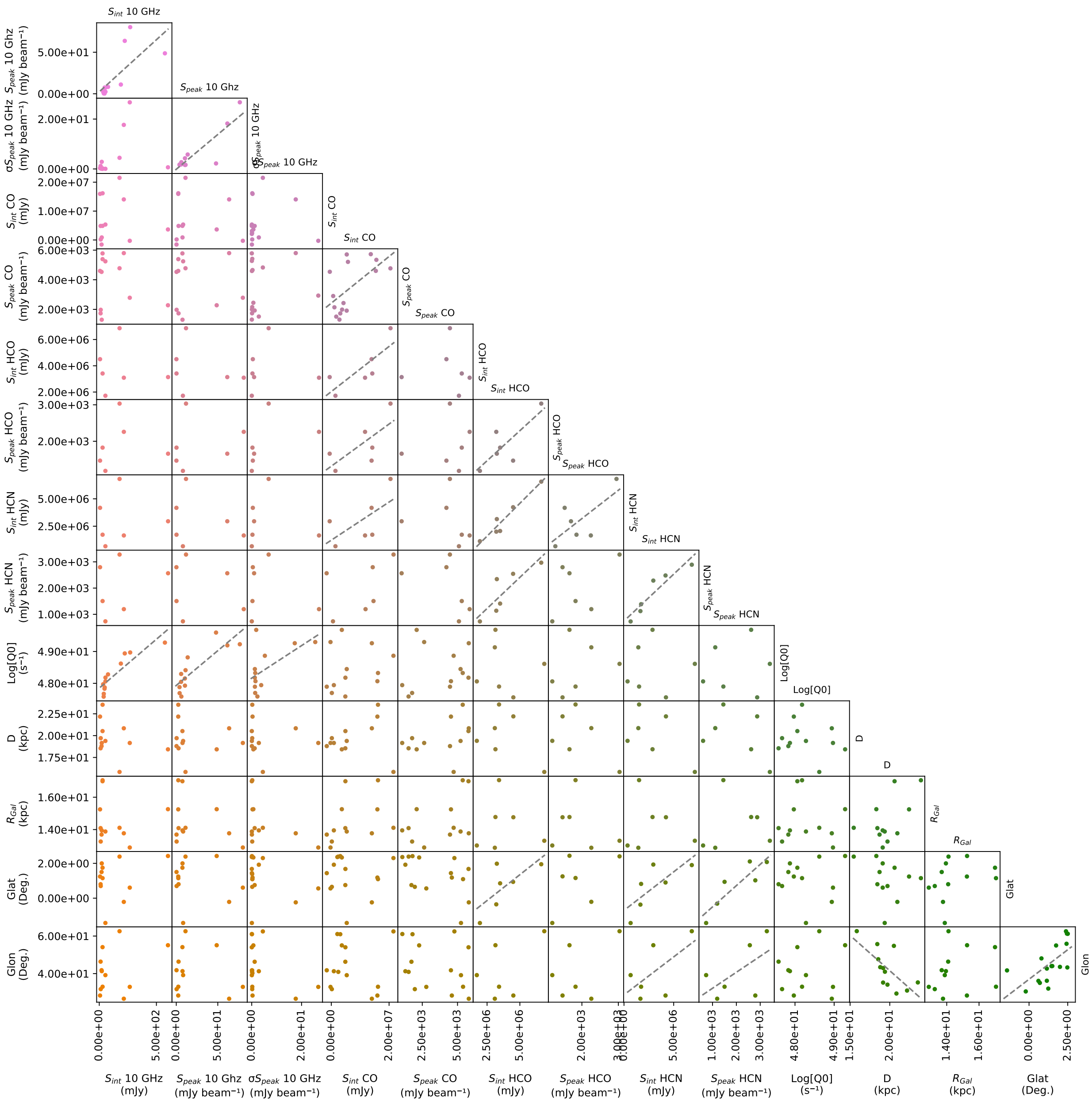

Figure 5. Data points include continuum and spectral line information from this study, Armentrout et al. (2017), and Armentrout et al. (2020) (*in prep*). Linear best-fit lines appear when they can account for 1/3 or more of the variance in the data ($R^2 \geqslant 0.33$). Data includes radio continuum emission from VLA20A-495, VLA14A-194, and Armentrout et al. (2017), as well as molecular gas data from the Argus instrument on the Green Bank Telescope, specifically CO, HCO, and HCN (GBT19A-460, GBT17B-431, GBT16B-420, GBT16A-414).

Figure 6. VLA Observations 20A-495.

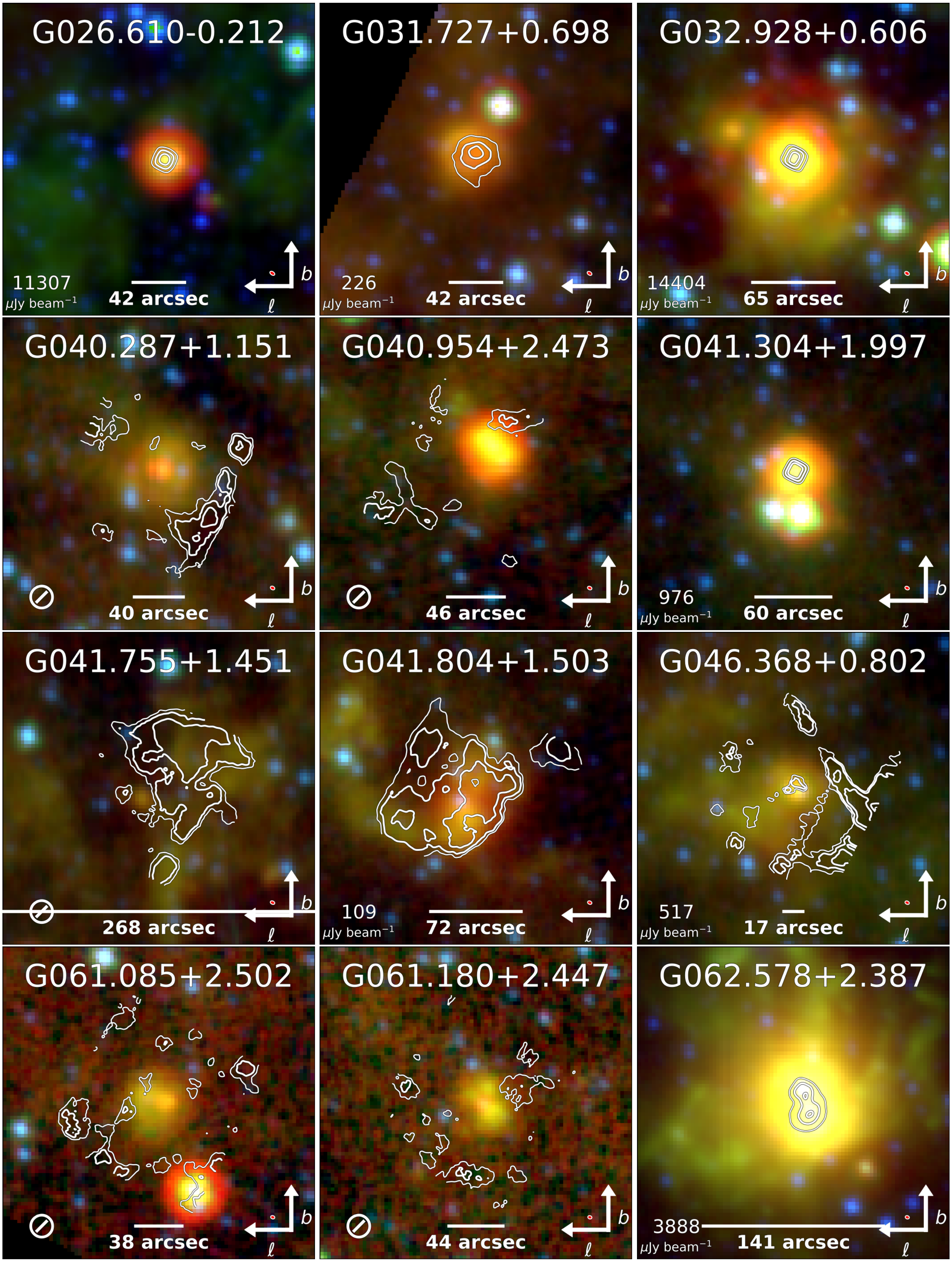

Figure 7. VLA Observations 14A-194 (Armentrout et al. 2017)